Open-Source Full-Waveform Ultrasound Computed Tomography Based on the Angular Spectrum Method Using Linear Arrays

Rehman Ali*

*Department of Electrical Engineering, Stanford University, Palo Alto, CA, 94305 USA

ABSTRACT

We present full-waveform ultrasound computed tomography (USCT) for sound speed reconstruction based on the angular spectrum method using linear transducer arrays. We first present a transmission scenario in which plane-waves are emitted by a transmitting array and received by an array on the opposite side of the object of interest. These arrays are rotated around the object of interest to interrogate the medium from different view angles. Waveform inversion reconstruction is demonstrated on a numerical breast phantom, in which sound speed is varied from 1486 to 1584 m/s. This example is used to isolate and examine the impact of each view angles and frequency used in the reconstruction process. We also examine cycle-skipping artifacts as well as optimization schemes that can be used to overcome them. The goal of this work is to provide an open-source example and implementation of the waveform inversion reconstruction algorithm on Github: https://github.com/rehmanali1994/FullWaveformInversionUSCT (DOI: 10.5281/zenodo.4774394). Next, we extend the waveform inversion framework to perform sound speed tomography for pulse-echo ultrasound imaging with a single linear array that transmits pulsed waves and receives signals backscattered from the medium. We first demonstrate that B-mode image reconstructions can be achieved using the angular spectrum method; then, we derive an optimization framework for estimating the sound speed in the medium by optimizing B-mode images with respect to slowness, via the angular spectrum method. We demonstrate an initial proof of concept with point targets in a homogeneous medium to demonstrate the fundamental principles of this new technique.

Keywords: Nonlinear inverse problems, waveform inversion, ultrasound, tomography, angular spectrum method

1. INTRODUCTION

Ultrasound computed tomography (USCT) is an imaging technique that uses the transmission of ultrasound through tissue to reconstruct high-resolution images of tissue properties such as sound speed and attenuation. The primary application of ultrasound tomography is in breast imaging[1–6] where sound speed and attenuation are key biomarkers for the identification of cancer in the breast. This report specifically investigates USCT for sound speed estimation in heterogeneous sound-speed media.

Techniques for sound speed estimation strategies generally fall into two broad categories: bent-ray methods,[7,8] and waveform inversion.[9,10] Waveform inversion appears to be the most accurate technique for USCT reconstruction and greatly outperforms bent-ray reconstructions in most applications. Despite the substantially lower computation time of bent-ray methods, their key drawback is the inability to account for diffraction, which inevitably leads to poorer resolution in the reconstructed image. Waveform inversion is more accurate because it uses iterative simulations of diffraction to estimate the sound speed profile responsible for producing the measured ultrasound signals.

This report specifically investigates waveform inversion for sound speed estimation in heterogeneous sound-speed media using USCT. The primary goal of this work is to demonstrate and examine each step of waveform inversion using the angular spectrum method.[11,12] We aim to examine the parameters that impact sound speed reconstruction and consider challenges posed by cycle skipping on a robust reconstruction algorithm. Although

Further author information: (Send correspondence to Rehman Ali)
Rehman Ali: E-mail: rali8@stanford.edu

Medical Imaging 2022: Ultrasonic Imaging and Tomography, edited by Nick Bottenus, Nicole V. Ruiter, Proc. of SPIE Vol. 12038, 120380R · © 2022 SPIE · 1605-7422 · doi: 10.1117/12.2601257

waveform inversion techniques for USCT have been well explored,[9,13,14] there is a lack of openly available codes that demonstrate waveform-inversion for USCT reconstruction.[15,16] With this implementation, we aim to provide an open-source example.

The secondary goal of this work is to extend the waveform inversion framework used in transmission USCT to perform sound speed estimation in pulse-echo ultrasound.[17–21] The angular spectrum method can be used reconstruct B-mode ultrasound images based on knowledge of the transmission sequence used to image the medium and the receive signals collected from each transmit event.[22–24] Because the B-mode image reconstruction is parameterized by the sound speed in the medium through the angular spectrum method, the same mathematical framework used to perform sound speed reconstruction in transmission USCT may be used to derive a sound speed estimation procedure for pulse echo ultrasound imaging. We aim to demonstrate the principles of this sound speed estimation technique for pulse-echo ultrasound imaging using a preliminary demonstration with point targets.

2. BACKGROUND

2.1 Fourier Split-Step Angular Spectrum Method

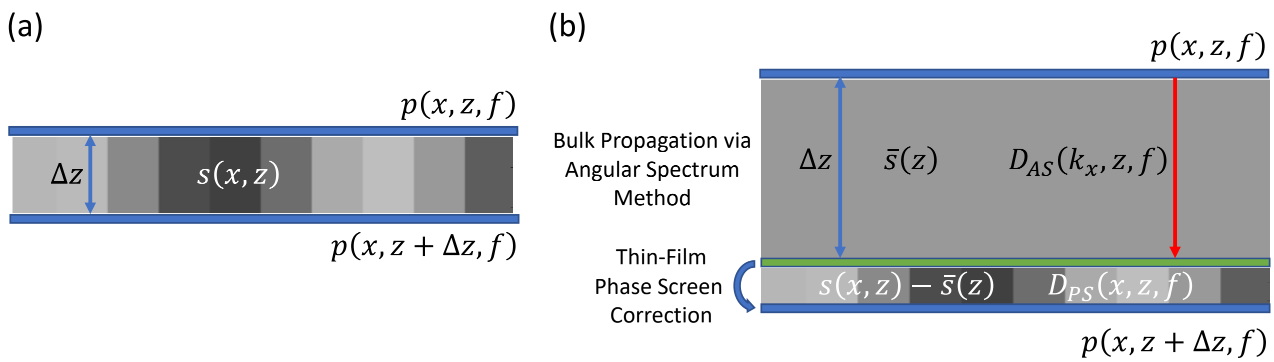

Figure 1. Fourier Split-Step Angular Spectrum Method for Simulating Ultrasonic Pressure Fields. (a) Propagation from depth z to $z + \Delta z$ in a heterogeneous slowness medium. (b) Decomposition of propagation into bulk propagation via the angular spectrum method followed by a correcting phase screen (see equations (1), (2), and (3)).

Ultrasonic wave-fields $p(x, z, f)$ as a function of location (x, z) and frequency f can be propagated from a depth of z to $z + \Delta z$ using the Fourier split-step form of the angular spectrum method

$$p(x, z + \Delta z, f) = D_{PS}(x, z, f)\mathcal{F}^{-1}_{k_x \leftarrow x}\{D_{AS}(k_x, z, f)\mathcal{F}_{x \leftarrow k_x}\{p(x, z, f)\}\}, \quad (1)$$

$$D_{AS}(k_x, z, f) = \exp\left(-j2\pi\Delta z\sqrt{\left(f\bar{s}(z)\right)^2 - k_x^2}\right), \quad (2)$$

$$D_{PS}(x, z, f) = \exp\left(-j2\pi f\Delta z\left(s(x, z) - \bar{s}(z)\right)\right), \quad (3)$$

where $\mathcal{F}_{x \leftarrow k_x}$ and $\mathcal{F}^{-1}_{k_x \leftarrow x}$ are the forward and inverse Fourier transforms in the lateral dimension (x), $s(x, z)$ is the slowness (i.e., the reciprocal of sound speed) at (x, z), and $\bar{s}(z)$ is the mean slowness at depth z. Bulk propagation $D_{AS}(k_x, z, f)$ via the angular spectrum (AS) method occurs in the k_x-domain. The phase screen (PS) correction $D_{PS}(x, z, f)$ occurs after the angular spectrum method and accounts for the laterally varying component of the slowness. These steps are shown visually in Figure 1.

Figure 2(a) illustrates a vector notation for the pressure field at each layer in the medium. Using this notation, the angular spectrum method can be represented as

$$\vec{p}_k(\vec{s}, f) = D_k(\vec{s}, f)\vec{p}_{k-1}(\vec{s}, f), \quad (4)$$

$$D_k(\vec{s}, f) = D_{PS,k}(\vec{s}, f)\mathcal{F}^* D_{AS,k}(\vec{s}, f)\mathcal{F}, \quad (5)$$

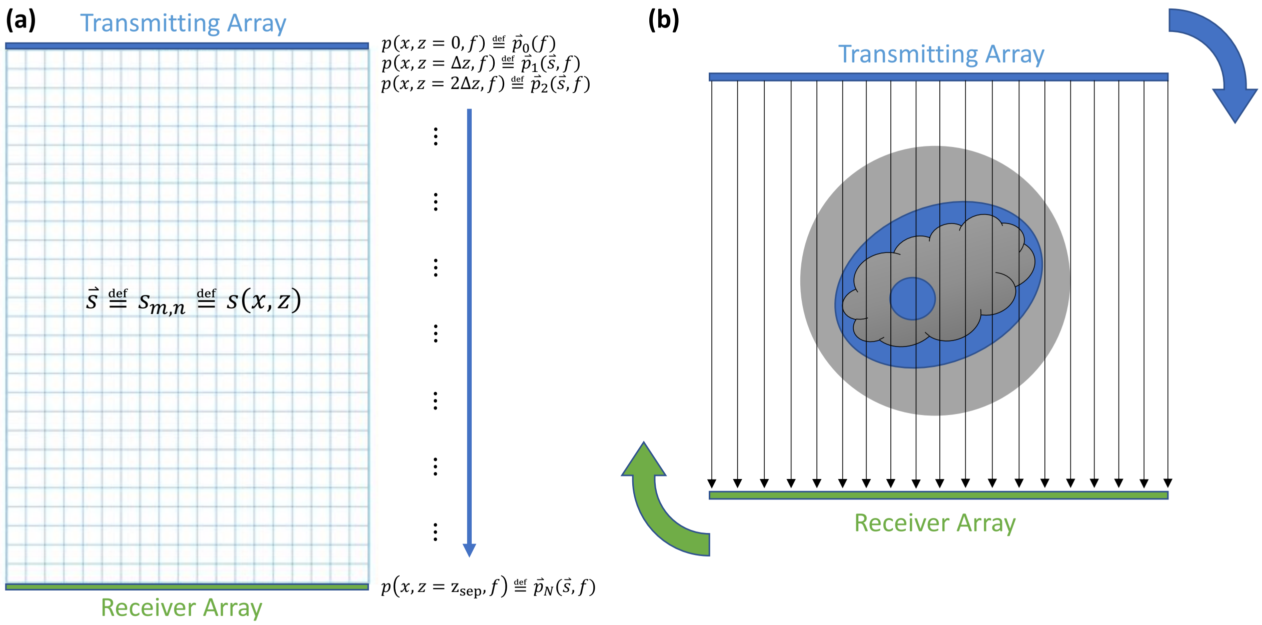

Figure 2. Plane-wave Transmission Simulation Geometry and Mathematical Notation. (a) This schematic shows a vectorization of the wavefields at each layer in the medium. The distance between the transmitting and receiving arrays is denoted as z_{sep}. The signals measured at the receiving array are used in full-waveform inversion. (b) The transmitting and receiving arrays are rotated around the medium. The received signals from each view angle are used in the complete full-waveform inversion.

where $\vec{s}$ is the vectorization of slowness values over the grid, $\mathcal{F}$ is the discrete Fourier transform matrix, $D_{AS,k}(\vec{s}, f)$ is the angular spectrum method as a diagonal matrix acting in the k_x domain, and $D_{PS,k}(\vec{s}, f)$ is the phase screen implemented as a diagonal matrix acting over the x domain. These recursive relations describe the downward propagation of the ultrasonic wave-field from the transmitting array to the receiving array. The entire Fourier split-step angular spectrum method for all layers in the medium can be summarized using the following matrix formulation:

$$A(\vec{s}, f)\vec{y}(\vec{s}, f) = \vec{b}(\vec{s}, f), \tag{6}$$

where

$$A(\vec{s}, f) = \begin{bmatrix} I & 0 & 0 & \dots & 0 & 0 \\ -D_1(\vec{s}, f) & I & 0 & \dots & 0 & 0 \\ 0 & -D_2(\vec{s}, f) & I & \dots & 0 & 0 \\ \vdots & \vdots & \vdots & \ddots & \vdots & \vdots \\ 0 & 0 & 0 & \dots & I & 0 \\ 0 & 0 & 0 & \dots & -D_N(\vec{s}, f) & I \end{bmatrix}, \tag{7}$$

$$\vec{y}(\vec{s}, f) = \begin{bmatrix} \vec{p}_0(f) \\ \vec{p}_1(\vec{s}, f) \\ \vec{p}_2(\vec{s}, f) \\ \vdots \\ \vec{p}_{N-1}(\vec{s}, f) \\ \vec{p}_N(\vec{s}, f) \end{bmatrix}, \qquad \vec{b}(\vec{s}, f) = \begin{bmatrix} \vec{p}_0(f) \\ \vec{0} \\ \vec{0} \\ \vdots \\ \vec{0} \\ \vec{0} \end{bmatrix}. \tag{8}$$

Note that the signal measured across the receiving arrays is $\vec{p}_N(\vec{s}, f) = K\vec{y}(\vec{s}, f)$ where $K = [0, \dots, 0, I]$; therefore, the received signals can be modeled as

$$\vec{p}_N(\vec{s}, f) = K[A(\vec{s}, f)]^{-1}\vec{b}(\vec{s}, f), \tag{9}$$

where $\vec{b}(\vec{s}, f)$ represents the signal injected at the transmitting array, $[A(\vec{s}, f)]^{-1}$ is the downward propagation of signals via the angular spectrum, and K samples this wave-field at the receiving array.

2.2 Derivation of the USCT Reconstruction Algorithm

Figure 2(a) illustrates the mathematical notation of the angular spectrum method and Figure 2(b) illustrates the geometry used when deriving full-waveform inversion procedure for this imaging problem. The angular spectrum method is used to (1) simulate received signals based on current estimates of slowness (i.e., the reciprocal of sound speed) in the medium and (2) back-project errors in the receive signals to create slowness updates. The complete objective function for full-waveform inversion is

$$\underset{\vec{s}}{\text{minimize}} \quad J(\vec{s}) = \frac{1}{2} \sum_{f} \sum_{i=1}^{N_{views}} \|\vec{p}_{N,i}(\vec{s}, f) - \vec{p}_{obs,i}(f)\|_2^2, \tag{10}$$

where the view angles around the imaged object are indexed $i = 1, ..., N_{views}$, $\vec{p}_{obs,i}(f)$ represents the observed receive signals from each view angle, and $\vec{p}_{N,i}(\vec{s}, f)$ represents the modeled receive signals based on the current estimate of the slowness $\vec{s}$.

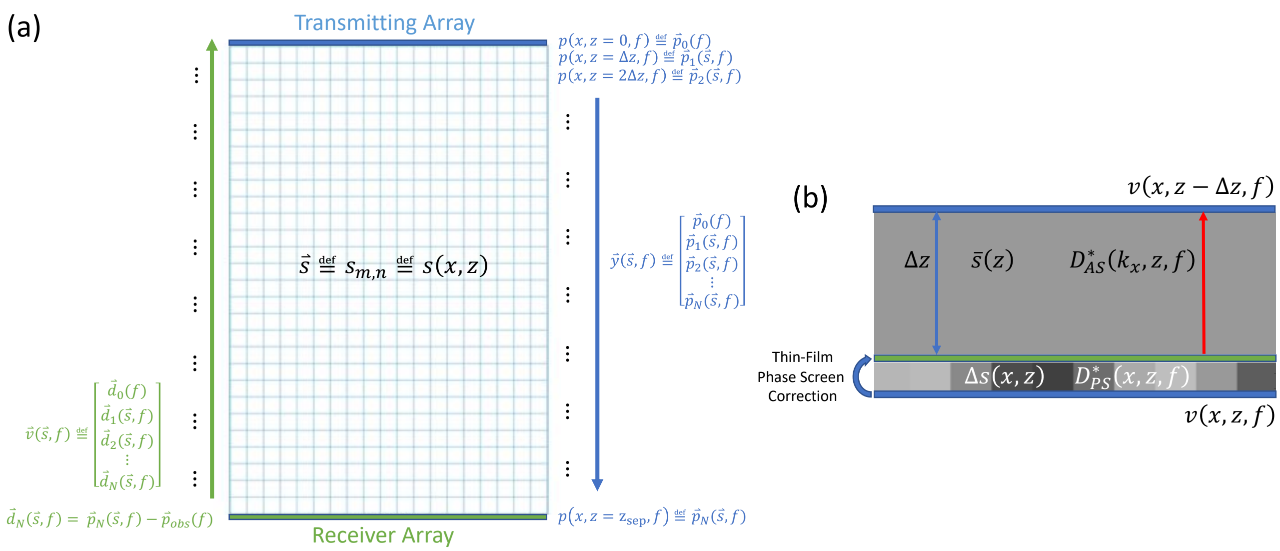

Figure 3. Upward Propagation of Adjoint Wave-Field. (a) This schematic shows a vectorization of the upward propagation of the error in the receive signals. (b) The angular spectrum method used in the upward propagation is mathematically adjoint (reversed in order and complex conjugated) to the downward propagation.

The goal of this section is to show a complete derivation of each step in the waveform inversion process. We first consider the partial objective function $J_i(\vec{s}, f) = \frac{1}{2}\|\vec{p}_{N,i}(\vec{s}, f) - \vec{p}_{obs,i}(f)\|_2^2$ at view i and frequency f. The gradient of this partial objective function with respect to the slowness $s_{m,n}$ at pixels (m, n) is

$$\frac{\partial J_i(\vec{s}, f)}{\partial s_{m,n}} = Re\left\{ (\vec{p}_{N,i}(\vec{s}, f) - \vec{p}_{obs,i}(f))^H \frac{\partial \vec{p}_{N,i}(\vec{s}, f)}{\partial s_{m,n}} \right\}, \tag{11}$$

where

$$\begin{aligned} \frac{\partial \vec{p}_{N,i}(\vec{s}, f)}{\partial s_{m,n}} &= \frac{\partial}{\partial s_{m,n}} \left(K[A(\vec{s}, f)]^{-1} \vec{b}(\vec{s}, f) \right) = K \frac{\partial [A(\vec{s}, f)]^{-1}}{\partial s_{m,n}} \vec{b}(\vec{s}, f) \\ &= -K[A(\vec{s}, f)]^{-1} \frac{\partial A(\vec{s}, f)}{\partial s_{m,n}} [A(\vec{s}, f)]^{-1} \vec{b}(\vec{s}, f) = -K[A(\vec{s}, f)]^{-1} \frac{\partial A(\vec{s}, f)}{\partial s_{m,n}} \vec{y}(\vec{s}, f). \end{aligned}$$

After further simplifications, this gradient may be expressed as

$$\frac{\partial J_i(\vec{s},f)}{\partial s_{m,n}} = Re\left\{-\vec{v}^H(\vec{s},f)\frac{\partial A(\vec{s},f)}{\partial s_{m,n}}\vec{y}(\vec{s},f)\right\}, \tag{12}$$

where

$$\vec{v}(\vec{s},f) = [A^H(\vec{s},f)]^{-1}K^T\left(\vec{p}_{N,i}(\vec{s},f) - \vec{p}_{obs,i}(f)\right). \tag{13}$$

While $\vec{y}(\vec{s},f)$ is the wave-field projected forward from the transmitting array, $\vec{v}(\vec{s},f)$ is a back-projection of the error between the modeled and measured signals at the receiver array upwards into the medium (see Figure 3(a)). Equation (13) shows that the error $\vec{p}_{N,i}(\vec{s},f) - \vec{p}_{obs,i}(f)$ is injected at the receiver array using the K^T operator (K represents sampling at the receiver array, so K^T is an injection operator). Then, the resulting injected error is propagated upwards using an adjoint form of the angular spectrum method via $[A^H(\vec{s},f)]^{-1}$. To see this, equation (13) can be re-written as

$$A^H(\vec{s},f)\vec{v}(\vec{s},f) = [0,\ldots,0,I]^T\left(\vec{p}_{N,i}(\vec{s},f) - \vec{p}_{obs,i}(f)\right), \tag{14}$$

$$\begin{bmatrix} I & -D_1^H(\vec{s},f) & 0 & \ldots & 0 & 0 \\ 0 & I & -D_2^H(\vec{s},f) & \ldots & 0 & 0 \\ 0 & 0 & I & \ldots & 0 & 0 \\ \vdots & \vdots & \vdots & \ddots & \vdots & \vdots \\ 0 & 0 & 0 & \ldots & I & -D_N^H(\vec{s},f) \\ 0 & 0 & 0 & \ldots & 0 & I \end{bmatrix} \begin{bmatrix} \vec{d}_0(f) \\ \vec{d}_1(\vec{s},f) \\ \vec{d}_2(\vec{s},f) \\ \vdots \\ \vec{d}_{N-1}(\vec{s},f) \\ \vec{d}_N(\vec{s},f) \end{bmatrix} = \begin{bmatrix} \vec{0} \\ \vec{0} \\ \vec{0} \\ \vdots \\ \vec{0} \\ \vec{p}_{N,i}(\vec{s},f) - \vec{p}_{obs,i}(f) \end{bmatrix}. \tag{15}$$

In recursive form, this is implemented as the upward propagation of the error between the modeled and observed receive signals (see Figure 3(b)):

$$\vec{d}_N(\vec{s},f) = \vec{p}_N(\vec{s},f) - \vec{p}_{obs}(f), \tag{16}$$

$$\vec{d}_{k-1}(\vec{s},f) = D_k^H(\vec{s},f)\vec{d}_k(\vec{s},f). \tag{17}$$

where

$$D_k(\vec{s},f) = \mathcal{F}^* D_{AS,k}^*(\vec{s},f)\mathcal{F} D_{PS,k}^*(\vec{s},f), \tag{18}$$

$$D_{AS}^*(k_x,z,f) = \exp\left(+j2\pi\Delta z\sqrt{\left(f\bar{s}(z)\right)^2 - k_x^2}\right), \tag{19}$$

$$D_{PS}^*(x,z,f) = \exp\left(+j2\pi f\Delta z\left(s(x,z) - \bar{s}(z)\right)\right). \tag{20}$$

Revisiting equation (12), we now look at the $\frac{\partial A(\vec{s},f)}{\partial s_{m,n}}$ term:

$$\frac{\partial A(\vec{s},f)}{\partial s_{m,n}} = \begin{bmatrix} 0 & 0 & 0 & \ldots & 0 & 0 \\ -\frac{\partial D_1(\vec{s},f)}{\partial s_{m,n}} & 0 & 0 & \ldots & 0 & 0 \\ 0 & -\frac{\partial D_2(\vec{s},f)}{\partial s_{m,n}} & 0 & \ldots & 0 & 0 \\ \vdots & \vdots & \vdots & \ddots & \vdots & \vdots \\ 0 & 0 & 0 & \ldots & 0 & 0 \\ 0 & 0 & 0 & \ldots & -\frac{\partial D_N(\vec{s},f)}{\partial s_{m,n}} & 0 \end{bmatrix}. \tag{21}$$

According to the Rytov approximation,[25,26] the phase screen can absorb all perturbations in the slowness so that

$$\frac{\partial D_k(\vec{s},f)}{\partial s_{m,n}} = \frac{\partial D_{PS,k}(\vec{s},f)}{\partial s_{m,n}}\mathcal{F}^* D_{AS,k}(\vec{s},f)\mathcal{F}. \tag{22}$$

The mathematical expression for the matrix form of the phase screen $D_{PS,k}(\vec{s},f)$ is

$$D_{PS,k}(\vec{s},f) = \operatorname*{diag}_{l}\{\exp\left(-j2\pi f(s_{l,k} - \bar{s}_l)\Delta z\right)\}. \tag{23}$$

The derivative of the phase screen with respect to $s_{m,n}$ is

$$\frac{\partial D_{PS,k}(\vec{s},f)}{\partial s_{m,n}} = \begin{cases} \underset{l}{\operatorname{diag}}\{0,...,0,-j2\pi f\Delta z \exp\left(-j2\pi f(s_{m,n}-\bar{s}_m)\Delta z\right),0,...,0\} & k=n \\ 0 & \text{otherwise} \end{cases}. \tag{24}$$

Based on equation (24), $\frac{\partial D_{PS,k}(\vec{s},f)}{\partial s_{m,n}}$ is a diagonal matrix with at most 1 non-zero element, which means that $\frac{\partial D_k(\vec{s},f)}{\partial s_{m,n}}$ is a diagonal matrix with at most 1 non-zero element. Ultimately, this means that $\frac{\partial A(\vec{s},f)}{\partial s_{m,n}}$ is a matrix with exactly 1 non-zero element corresponding to the voxel for $s_{m,n}$. This implies that equation (12) represents a point-wise multiplication of the downward-going transmitted wave-field $\vec{y}(\vec{s},f)$ and the upward-going back-projected wave-field $\vec{v}(\vec{s},f)$ of the error in the received signals. Following this line of reasoning, if we denote $\circ$ as the point-wise multiplication of two vectors (i.e., $\begin{bmatrix} a_1 \\ a_2 \\ a_3 \end{bmatrix} \circ \begin{bmatrix} b_1 \\ b_2 \\ b_3 \end{bmatrix} = \begin{bmatrix} a_1 b_1 \\ a_2 b_2 \\ a_3 b_3 \end{bmatrix}$), then

$$\nabla_{\vec{s}} J_i(\vec{s},f) = Re\left\{-\vec{v}^*(\vec{s},f) \circ \left(-j2\pi f\Delta z\left(A(\vec{s},f)-I\right)\vec{y}(\vec{s},f)\right)\right\}, \tag{25}$$

where $-j2\pi f\Delta z\left(A(\vec{s},f)-I\right)$ is equivalent to the $\frac{\partial A(\vec{s},f)}{\partial s_{m,n}}$ term from before. Further simplifications yield

$$\begin{aligned} \nabla_{\vec{s}} J_i(\vec{s},f) &= Re\left\{\vec{v}^*(\vec{s},f) \circ \left(-j2\pi f\Delta z\left(I-A(\vec{s},f)\right)\vec{y}(\vec{s},f)\right)\right\} \\ &= Re\left\{-j2\pi f\Delta z\left(\vec{v}^*(\vec{s},f) \circ \left(\vec{y}(\vec{s},f)-\vec{b}(f)\right)\right)\right\}. \end{aligned} \tag{26}$$

However, because $\vec{b}(f)$ is zero wherever a slowness pixel exists, the gradient of the partial objective function is

$$\nabla_{\vec{s}} J_i(\vec{s},f) = Re\left\{-j2\pi f\Delta z\left(\vec{v}^*(\vec{s},f) \circ \vec{y}(\vec{s},f)\right)\right\}. \tag{27}$$

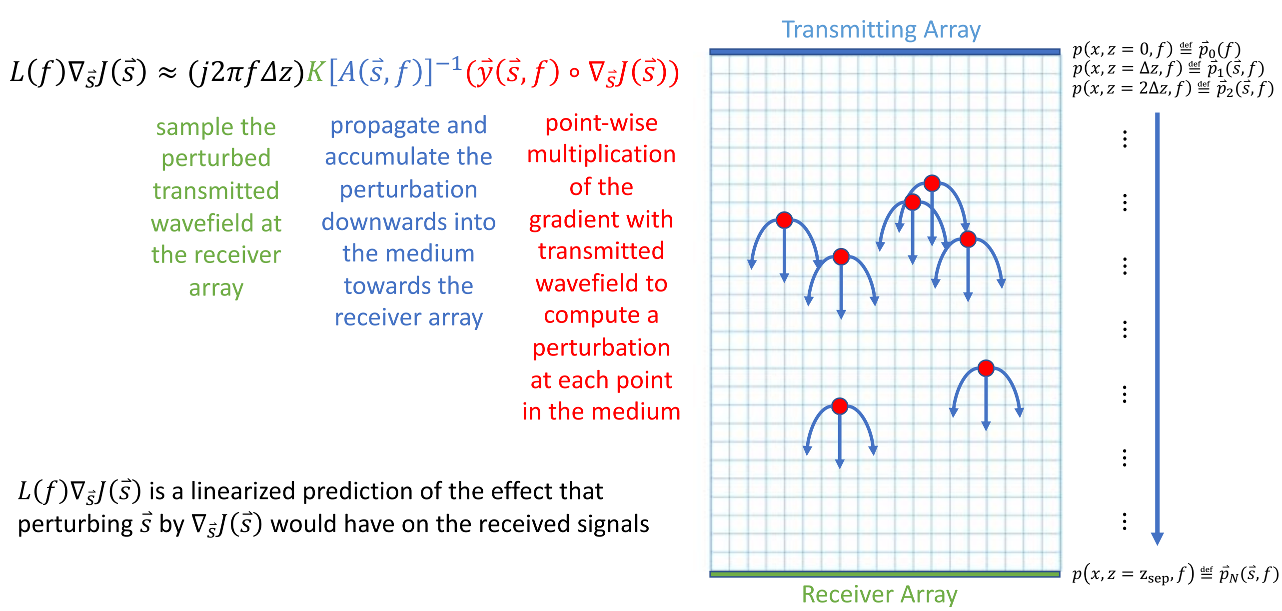

Figure 4. Visual Interpretation of $L(f)\nabla_{\vec{s}}J(\vec{s})$ Representing the Linearized Forward Projection of Gradient $\nabla_{\vec{s}}J(\vec{s})$ on the Received Ultrasound Signal.

A fast and robust conjugate gradient (CG) algorithm for the minimization problem (10) requires a fast and closed-form solution for the step length of $\nabla_{\vec{s}}J(\vec{s})$. This requires a linearization $L_i(f)$ around the current slowness such that $J_i(\vec{s}, f) = \frac{1}{2}\|\vec{p}_{N,i}(\vec{s}, f) - \vec{p}_{obs,i}(f)\|_2^2 = \frac{1}{2}\|L_i(f)\vec{s} - \vec{p}_{obs,i}(f)\|_2^2$ can be expressed as a linearized least-squares minimization problem. Assuming there is a linearization $L_i(f)$ around the current slowness estimate $\vec{s}$, the partial gradients would be $\nabla_{\vec{s}} J_i(\vec{s}, f) = L_i^H(f)\left(L_i(f)\vec{s} - \vec{p}_{obs,i}(f)\right)$. Note that these partial gradients $\nabla_{\vec{s}} J_i(\vec{s}, f)$ would be summed over all view angles and frequencies to compute the complete gradient $\nabla_{\vec{s}} J(\vec{s})$: $\nabla_{\vec{s}} J(\vec{s}) = \sum_f \sum_{i=1}^{N_{views}} \nabla_{\vec{s}} J_i(\vec{s}, f)$. To implement the CG algorithm for this problem, the step length calculation requires computing $L_i(f)\nabla_{\vec{s}} J(\vec{s})$. Note that $L_i(f)$ is simply $\frac{\partial \vec{p}_{N,i}(\vec{s}, f)}{\partial \vec{s}}$ from equation (2.2) so that

$$L_i(f) = \frac{\partial \vec{p}_{N,i}(\vec{s}, f)}{\partial \vec{s}} = -K[A(\vec{s}, f)]^{-1} \frac{\partial A(\vec{s}, f)}{\partial \vec{s}} \vec{y}(\vec{s}, f),$$

and

$$L_i(f)\nabla_{\vec{s}} J(\vec{s}) = (j2\pi f \Delta z) K [A(\vec{s}, f)]^{-1} \left(\vec{y}(\vec{s}, f) \circ \nabla_{\vec{s}} J(\vec{s})\right).$$

Figure 4 shows a visual interpretation of equation (2.2): $L_i(f)\nabla_{\vec{s}} J(\vec{s})$ represents a linearized prediction of the the effect that perturbing $\vec{s}$ by $\nabla_{\vec{s}} J(\vec{s})$ would have on receive signals $\vec{p}_{N,i}(\vec{s}, f)$.

Composing all the key components of the gradient calculation and the linearized forward projection of the gradient, the CG algorithm for the spatial reconstruction of slowness is described in Algorithm 1. Note that the CG algorithm is intentionally dampened by the γ parameter to overcome issues related to cycle-skipping, which we demonstrate and discuss in more details later on.

Algorithm 1 Conjugate Gradient (CG) Algorithm for Waveform Inversion Reconstruction of Slowness

1: Initialize slowness $\vec{s}_0$ to a uniform profile: $\vec{s}_0 = s_{init}\vec{1}$ ▷ $s_{init} = \frac{1}{1540\frac{m}{s}}$
2: Initialize search direction $\vec{d}_0 = -\nabla_{\vec{s}} J(\vec{s}_0)$
3: Initialize step length parameter $\gamma \leq 1$ ▷ $\gamma << 1$ to dampen CG for cycle-skipping problem
4: **for** $k = 0, ..., N-1$ **do** ▷ N Iterations of CG
5: Compute Step Size: $\alpha_k = -\gamma \frac{\vec{d}_k^T \nabla_{\vec{s}} J(\vec{s}_k)}{\sum_f \sum_{i=1}^{N_{views}} \|L_i(f)\vec{d}_k\|_2^2}$.
6: Update Slowness: $\vec{s}_{k+1} = \vec{s}_k + \alpha_k \vec{d}_k$
7: Compute Momentum: $\beta_k = \min\left(\max\left(\frac{\nabla_{\vec{s}} J(\vec{s}_{k+1})^T(\nabla_{\vec{s}} J(\vec{s}_{k+1}) - \nabla_{\vec{s}} J(\vec{s}_k))}{\nabla_{\vec{s}} J(\vec{s}_k)^T \nabla_{\vec{s}} J(\vec{s}_k)}, 0\right), \frac{\nabla_{\vec{s}} J(\vec{s}_{k+1})^T \nabla_{\vec{s}} J(\vec{s}_{k+1})}{\nabla_{\vec{s}} J(\vec{s}_k)^T \nabla_{\vec{s}} J(\vec{s}_k)}\right)$
8: Update Search Direction: $\vec{d}_{k+1} = -\nabla_{\vec{s}} J(\vec{s}_{k+1}) + \beta_k \vec{d}_k$
9: **end for**
10: **return** $\vec{s}_N$

2.3 Pulse-Echo Ultrasound Imaging Based on the Angular Spectrum Method

Pulse-echo ultrasound images can be created by propagating transmit and receive wavefields $p_{tx(i)}(x, z, f)$ and $p_{rx(i)}(x, z, f)$ based on the transmit sequence and receive channel data collected from each transmit event $i = 1, ..., N_{tx}$.[22–24] Partial images $I_i(x, z)$ prior to amplitude detection can be formed by cross correlating the transmit and receive wavefields:

$$I_i(x, z) = \int_0^\infty p_{tx(i)}^*(x, z, f) p_{rx(i)}(x, z, f) df, \tag{28}$$

$$p_{tx(i)}(x, z + \Delta z, f) = D_{PS}(x, z, f)\mathcal{F}_{k_x \leftarrow x}^{-1}\{D_{AS}(k_x, z, f)\mathcal{F}_{x \leftarrow k_x}\{p(x, z, f)\}\}, \tag{29}$$

$$p_{rx(i)}(x, z + \Delta z, f) = D_{PS}^*(x, z, f)\mathcal{F}_{k_x \leftarrow x}^{-1}\{D_{AS}^*(k_x, z, f)\mathcal{F}_{x \leftarrow k_x}\{p(x, z, f)\}\}. \tag{30}$$

If we vectorize $I_i(x, z)$, $p_{tx(i)}(x, z, f)$, and $p_{rx(i)}(x, z, f)$ as $\vec{I}_i(\vec{s})$, $\vec{y}_{tx(i)}(\vec{s}, f)$, and $\vec{y}_{rx(i)}(\vec{s}, f)$, the image formation process can be expressed as

$$\vec{I}_i(\vec{s}) = \int_0^\infty \vec{y}_{tx(i)}^*(\vec{s}, f) \circ \vec{y}_{rx(i)}(\vec{s}, f) df, \tag{31}$$

$$\vec{y}_{tx(i)}(\vec{s}, f) = [A(\vec{s}, f)]^{-1} \vec{b}_{tx(i)}(\vec{s}, f), \tag{32}$$

$$\vec{y}_{rx(i)}(\vec{s},f) = [A^*(\vec{s},f)]^{-1}\vec{b}_{rx(i)}(\vec{s},f), \tag{33}$$

where $\vec{b}_{tx(i)}(\vec{s},f)$ and $\vec{b}_{rx(i)}(\vec{s},f)$ represent the transmitted and recorded receive signals at the transducer surface consistent with the notation in equation (8).

2.4 Migration Velocity Analysis for Pulse-Echo Ultrasound Imaging

Wave-equation migration velocity analysis (WEMVA)[27–29] is a seismic imaging technique that reconstructs the slowness in the medium based on migrated images $I_i(x,z)$. Because the image formation process is parameterized by the slowness in the medium via the wave propagation model, the same theory used in waveform inversion can be used to derive slowness updates from the migrated images. In WEMVA, the image formation process in equation (31) can be linearized with respect to slowness:

$$\vec{I}_i(\vec{s}+\Delta\vec{s}) \approx \vec{I}_i(\vec{s}) + \frac{\partial \vec{I}_i(\vec{s})}{\partial \vec{s}}\Delta\vec{s}, \tag{34}$$

$$\frac{\partial \vec{I}_i(\vec{s})}{\partial \vec{s}} = \int_0^\infty \frac{\partial \vec{y}^*_{tx(i)}(\vec{s},f)}{\partial \vec{s}} \circ \vec{y}_{rx(i)}(\vec{s},f) + \vec{y}^*_{tx(i)}(\vec{s},f) \circ \frac{\partial \vec{y}_{rx(i)}(\vec{s},f)}{\partial \vec{s}} df, \tag{35}$$

where

$$\begin{aligned}
\frac{\partial \vec{y}_{tx(i)}(\vec{s},f)}{\partial \vec{s}} &= \frac{\partial [A(\vec{s},f)]^{-1}}{\partial \vec{s}}\vec{b}_{tx(i)}(\vec{s},f) \\
&= -[A(\vec{s},f)]^{-1}\frac{\partial A(\vec{s},f)}{\partial \vec{s}}[A(\vec{s},f)]^{-1}\vec{b}_{tx(i)}(\vec{s},f) \\
&= -[A(\vec{s},f)]^{-1}\frac{\partial A(\vec{s},f)}{\partial \vec{s}}\vec{y}_{tx(i)}(\vec{s},f),
\end{aligned} \tag{36}$$

$$\begin{aligned}
\frac{\partial \vec{y}_{rx(i)}(\vec{s},f)}{\partial \vec{s}} &= \frac{\partial [A^*(\vec{s},f)]^{-1}}{\partial \vec{s}}\vec{b}_{rx(i)}(\vec{s},f) \\
&= -[A^*(\vec{s},f)]^{-1}\frac{\partial A^*(\vec{s},f)}{\partial \vec{s}}[A^*(\vec{s},f)]^{-1}\vec{b}_{rx(i)}(\vec{s},f) \\
&= -[A^*(\vec{s},f)]^{-1}\frac{\partial A^*(\vec{s},f)}{\partial \vec{s}}\vec{y}_{rx(i)}(\vec{s},f).
\end{aligned} \tag{37}$$

The following equations show how to apply $\left(\frac{\partial \vec{I}_i(\vec{s})}{\partial \vec{s}}\right)^H$ to an image $\vec{I}(\vec{s})$:

$$\begin{aligned}
\left(\frac{\partial \vec{I}_i(\vec{s})}{\partial \vec{s}}\right)^H \vec{I}(\vec{s}) &= \left(\int_0^\infty \frac{\partial \vec{y}_{tx(i)}(\vec{s},f)}{\partial \vec{s}} \circ \vec{y}^*_{rx(i)}(\vec{s},f) + \vec{y}_{tx(i)}(\vec{s},f) \circ \frac{\partial \vec{y}^*_{rx(i)}(\vec{s},f)}{\partial \vec{s}} df\right)^T \vec{I}(\vec{s}) \\
&= \int_0^\infty \left(\frac{\partial \vec{y}_{tx(i)}(\vec{s},f)}{\partial \vec{s}}\right)^T \left(\vec{I}(\vec{s}) \circ \vec{y}^*_{rx(i)}(\vec{s},f)\right) + \left(\frac{\partial \vec{y}_{rx(i)}(\vec{s},f)}{\partial \vec{s}}\right)^H \left(\vec{I}(\vec{s}) \circ \vec{y}_{tx(i)}(\vec{s},f)\right) df,
\end{aligned} \tag{38}$$

where

$$\left(\frac{\partial \vec{y}_{tx(i)}(\vec{s},f)}{\partial \vec{s}}\right)^T = -\vec{y}^T_{tx(i)}(\vec{s},f)\left(\frac{\partial A(\vec{s},f)}{\partial \vec{s}}\right)^T [A(\vec{s},f)]^{-1}, \tag{39}$$

$$\left(\frac{\partial \vec{y}_{rx(i)}(\vec{s},f)}{\partial \vec{s}}\right)^H = -\vec{y}^H_{rx(i)}(\vec{s},f)\left(\frac{\partial A(\vec{s},f)}{\partial \vec{s}}\right)^T [A(\vec{s},f)]^{-1}. \tag{40}$$

Given a slowness perturbation $\Delta\vec{s}$, the image perturbation $\Delta\vec{I}_i(\vec{s})$ with respect to slowness may be computed as:

$$\Delta\vec{I}_i(\vec{s}) = \left(\frac{\partial \vec{I}_i(\vec{s})}{\partial \vec{s}}\right)\Delta\vec{s} = \int_0^\infty \left(\frac{\partial \vec{y}^*_{tx(i)}(\vec{s},f)}{\partial \vec{s}}\Delta\vec{s}\right) \circ \vec{y}_{rx(i)}(\vec{s},f) + \vec{y}^*_{tx(i)}(\vec{s},f) \circ \left(\frac{\partial \vec{y}_{rx(i)}(\vec{s},f)}{\partial \vec{s}}\Delta\vec{s}\right) df, \tag{41}$$

where

$$\frac{\partial \vec{y}_{tx(i)}(\vec{s},f)}{\partial \vec{s}}\Delta\vec{s} = -[A(\vec{s},f)]^{-1}\left(\frac{\partial A(\vec{s},f)}{\partial \vec{s}}\Delta\vec{s}\right)\vec{y}_{tx(i)}(\vec{s},f), \tag{42}$$

$$\frac{\partial \vec{y}_{rx(i)}(\vec{s},f)}{\partial \vec{s}}\Delta\vec{s} = -[A^*(\vec{s},f)]^{-1}\left(\frac{\partial A^*(\vec{s},f)}{\partial \vec{s}}\Delta\vec{s}\right)\vec{y}_{rx(i)}(\vec{s},f). \tag{43}$$

One approach to WEMVA for pulse-echo ultrasound is to maximize the B-mode image brightness. In pulse-echo ultrasound, the images $I_i(x,z)$ from each transmit event are coherently compounded, amplitude detected, and log-compressed into a B-mode ultrasound image: $I_{BMode}(x,z) = 20\log_{10}|\sum_{i=1}^{N_{tx}} I_i(x,z)|$. Maximizing $I_{BMode}(x,z)$ is conceptually equivalent to maximizing the power of the coherent sum of the images (as is often done in seismic imaging): $I_{power}(x,z) = \frac{1}{2}\left|\sum_{i=1}^{N_{tx}} I_i(x,z)\right|^2$ or $J_{power}(\vec{s}) = \frac{1}{2}\left\|\sum_{i=1}^{N_{tx}} \vec{I}_i(\vec{s})\right\|_2^2$. In this case, the gradient of the power of the coherent sum of migrated images with respect to the slowness is

$$\nabla_{\vec{s}} J_{power}(\vec{s}) = \sum_{i=1}^{N_{tx}} Re\left\{\left(\frac{\partial \vec{I}_i(\vec{s})}{\partial \vec{s}}\right)^H \left(\sum_{j=1}^{N_{tx}} \vec{I}_j(\vec{s})\right)\right\}. \tag{44}$$

However, the objective function here is not a least-squares minimization problem. In fact, the objective function is the maximization of a squared norm. Because the maximization of image brightness is not a least-squares problem, there is no forward model to linearize that would enable the closed form solution for the step size in a CG algorithm.

Algorithm 2 Conjugate Gradient (CG) Algorithm for Linearized WEMVA[30] Reconstruction of Slowness

Initialize slowness $\vec{s}_0$ to a uniform profile: $\vec{s}_0 = s_{init}\vec{1}$ ▷ $s_{init} = \frac{1}{1540\frac{m}{s}}$
Initialize step length parameter $\gamma \leq 1$ ▷ $\gamma << 1$ to dampen CG for cycle-skipping problem
for $n = 0, ..., N-1$ **do** ▷ N Updates to Slowness Model
  Compute all wavefields $\vec{y}_{tx(i)}$ and $\vec{y}_{rx(i)}$, and images $\vec{I}_i$ based on current slowness model $\vec{s}_n$
  Initialize slowness update $\Delta\vec{s}_0$ to zero: $\Delta\vec{s}_0 = \vec{0}$
  Initialize search direction $\vec{d}_0 = -\nabla_{\Delta\vec{s}} J(\Delta\vec{s}_0)$ ▷ J_{power} could be substituted for J
  for $k = 0, ..., K-1$ **do** ▷ K Iterations of CG
    Compute Step Size: $\alpha_k = -\gamma\frac{\vec{d}_k^T \nabla_{\Delta\vec{s}} J(\Delta\vec{s}_k)}{\sum_{i=1}^{N_{tx}} \|L_i \vec{d}_k\|_2^2}$ where $L_i = \left(\frac{\partial \vec{I}_{i+1}}{\partial \vec{s}} - \frac{\partial \vec{I}_i}{\partial \vec{s}}\right)$.
    Increment Slowness Update: $\Delta\vec{s}_{k+1} = \Delta\vec{s}_k + \alpha_k \vec{d}_k$
    Momentum: $\beta_k = \min\left(\max\left(\frac{\nabla_{\Delta\vec{s}} J(\Delta\vec{s}_{k+1})^T(\nabla_{\Delta\vec{s}} J(\Delta\vec{s}_{k+1}) - \nabla_{\Delta\vec{s}} J(\Delta\vec{s}_k))}{\Delta\nabla_{\vec{s}} J(\Delta\vec{s}_k)^T \nabla_{\Delta\vec{s}} J(\Delta\vec{s}_k)}, 0\right), \frac{\nabla_{\Delta\vec{s}} J(\Delta\vec{s}_{k+1})^T \nabla_{\Delta\vec{s}} J(\Delta\vec{s}_{k+1})}{\nabla_{\Delta\vec{s}} J(\Delta\vec{s}_k)^T \nabla_{\Delta\vec{s}} J(\Delta\vec{s}_k)}\right)$
    Update Search Direction: $\vec{d}_{k+1} = -\nabla_{\Delta\vec{s}} J(\Delta\vec{s}_{k+1}) + \beta_k \vec{d}_k$
  end for
  Update Slowness Model: $\vec{s}_{n+1} = \vec{s}_n + \Delta\vec{s}_K$
end for
return $\vec{s}_N$

A linearized approach to WEMVA[30] attempts to model the differences between migrated images from neighboring transmission events based on the underlying slowness. Specifically, this requires the assumption that $\vec{I}_i(\vec{s}) \approx \vec{I}_{i+\frac{1}{2}}(\vec{s}) \approx \vec{I}_{i+1}(\vec{s})$ so that any difference between $\vec{I}_i(\vec{s})$ and $\vec{I}_{i+1}(\vec{s})$ is solely due to an erroneous slowness model. The $\vec{I}_{i+\frac{1}{2}}(\vec{s})$ term is simply a notation device to express the similarity of images from neighboring transmit events. Using this notation, the differences $\vec{I}_{i+1}(\vec{s}) - \vec{I}_i(\vec{s})$ can be modeled by the slowness in the medium:

$$\vec{I}_i(\vec{s}+\Delta\vec{s}) \approx \vec{I}_i(\vec{s}) + \frac{\partial \vec{I}_i(\vec{s})}{\partial \vec{s}}\Delta\vec{s} \approx \vec{I}_{i+\frac{1}{2}}(\vec{s}) + \frac{\partial \vec{I}_i(\vec{s})}{\partial \vec{s}}\Delta\vec{s}, \tag{45}$$

$$\vec{I}_{i+1}(\vec{s}+\Delta\vec{s}) \approx \vec{I}_{i+1}(\vec{s}) + \frac{\partial \vec{I}_{i+1}(\vec{s})}{\partial \vec{s}}\Delta\vec{s} \approx \vec{I}_{i+\frac{1}{2}}(\vec{s}) + \frac{\partial \vec{I}_{i+1}(\vec{s})}{\partial \vec{s}}\Delta\vec{s}, \tag{46}$$

$$\vec{I}_{i+1}(\vec{s}+\Delta\vec{s}) - \vec{I}_i(\vec{s}+\Delta\vec{s}) \approx \left(\frac{\partial \vec{I}_{i+1}(\vec{s})}{\partial \vec{s}} - \frac{\partial \vec{I}_i(\vec{s})}{\partial \vec{s}}\right)\Delta\vec{s}. \tag{47}$$

This allows us to formulate the following linearized least-squares objective function and compute its gradient:

$$J(\Delta\vec{s}) = \frac{1}{2}\sum_{i=1}^{N_{tx}-1}\left\| \left(\frac{\partial \vec{I}_{i+1}}{\partial \vec{s}} - \frac{\partial \vec{I}_i}{\partial \vec{s}}\right)\Delta\vec{s} - \left(\vec{I}_{i+1} - \vec{I}_i\right)\right\|_2^2, \tag{48}$$

$$\nabla_{\Delta\vec{s}} J(\Delta\vec{s}) = \sum_{i=1}^{N_{tx}-1} Re\left\{\left(\frac{\partial \vec{I}_{i+1}}{\partial \vec{s}} - \frac{\partial \vec{I}_i}{\partial \vec{s}}\right)^H \left(\left(\frac{\partial \vec{I}_{i+1}}{\partial \vec{s}} - \frac{\partial \vec{I}_i}{\partial \vec{s}}\right)\Delta\vec{s} - \left(\vec{I}_{i+1} - \vec{I}_i\right)\right)\right\}. \tag{49}$$

Algorithm 2 summarizes a complete implementation of WEMVA[30] based on the conjugate gradient algorithm. However, because of the computational cost of WEMVA, this work only demonstrates the results of the first gradient computation (equations (44) and (49)) in the algorithm as an initial proof of concept. In a future work, we aim to provide a complete demonstration with a computationally-efficient implementation of WEMVA.

3. EXPERIMENTAL METHODS

3.1 USCT Simulation and Reconstruction

Figure 5 shows the ground-truth sound speed map from a numerical breast phantom and transmit pulse used to simulate receive signals in k-Wave. This sound speed map was adapted and modified from a contrast-enhanced cone-beam breast CT image in work from the Diagnostic Breast Center Göttingen (https://doi.org/10.1016/j.tranon.2017.08.010)[31] under the Creative Commons Attribution-NonCommercial-No Derivatives License (CC BY NC ND) (https://creativecommons.org/licenses/by-nc-nd/4.0/). Plane waves (pulse bandwidth: 0.5-1.5 MHz) are transmitted through the tissue from a transmitting linear array (192 elements, 0.6 mm pitch) to a receiving linear array (192 elements, 0.6 mm pitch). The distance between these arrays is z_{sep}=120 mm. These arrays are rotated 360 degrees around the medium in 2-degree steps. The reconstruction algorithms described in Algorithm 1 and section 2.2 of the Theory are used to reconstruct the speed of sound in the medium. The root-mean-square (RMS) error was used to estimate the accuracy of the sound speed reconstruction. The reconstruction is also decomposed into different frequencies and projection angles to analyze the methodology.

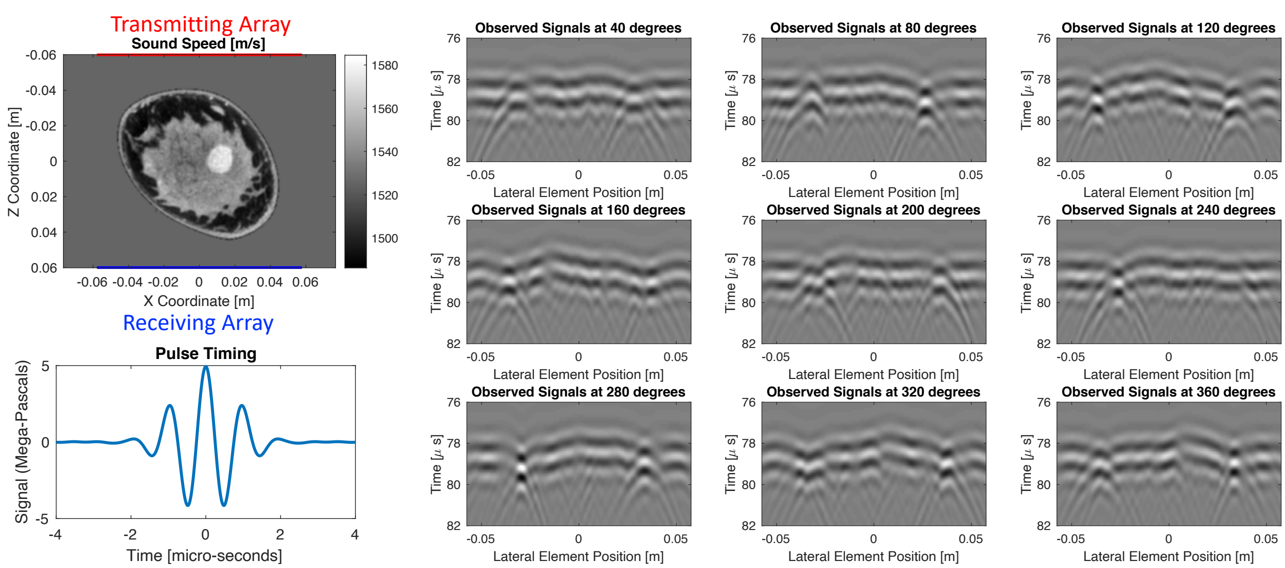

Figure 5. Numerical breast phantom. Sound speed map [m/s], transmit pulse, and k-Wave simulated receive signals from 9 different view angles. The sound speed map was adapted and modified from a contrast-enhanced cone-beam breast CT image in work from the Diagnostic Breast Center Göttingen (https://doi.org/10.1016/j.tranon.2017.08.010)[31] under the Creative Commons Attribution-NonCommercial-No Derivatives License (CC BY NC ND) (https://creativecommons.org/licenses/by-nc-nd/4.0/)

3.2 WEMVA Demonstration with Point Target Simulation

In this work, we apply a multistatic synthetic aperture sequence (96 element array, 0.25 mm pitch, 3.5 MHz center frequency, 70% fractional bandwidth) to a Field II-simulated point target at 30 mm depth in a 1540 m/s sound speed medium as an initial proof-of-concept for WEMVA. Equations (44) is first used to show the wave paths resulting from the individual transmit elements in the summation (i.e., $Re\left\{\left(\frac{\partial \vec{I}_i(\vec{s})}{\partial \vec{s}}\right)^H \left(\sum_{j=1}^{N_{tx}} \vec{I}_j(\vec{s})\right)\right\}$) when the point target is optimally focused at 1540 m/s using imaging technique described by section (2.3) of the Theory in order to show the wave-equivalent paths induced by WEMVA. Equations (44) and (49) are then used to construct gradient images when there is -4%, 0%, and +4% error between the initial sound speed guess and the ground truth of 1540 m/s.

4. NUMERICAL RESULTS

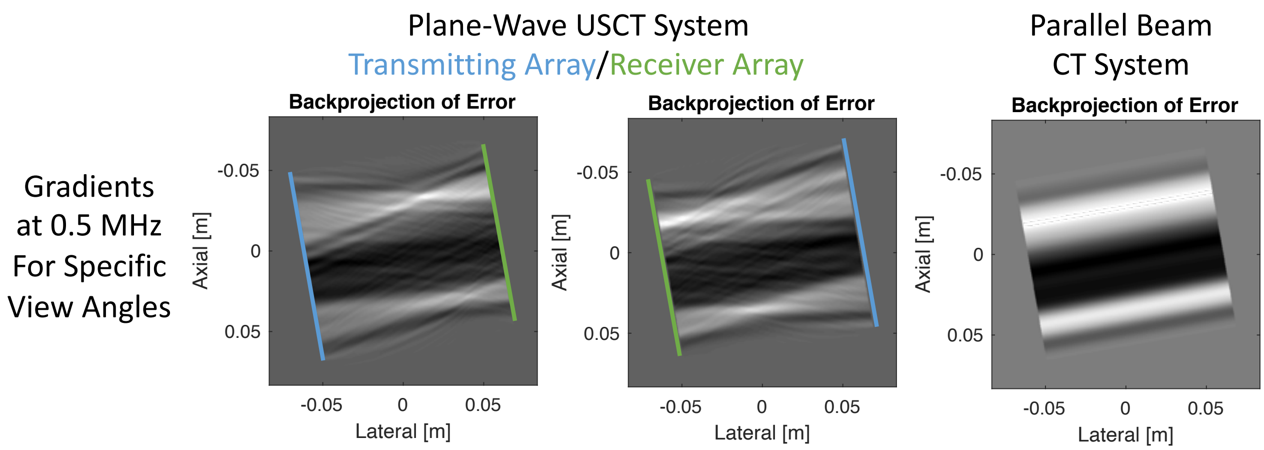

Figure 6. Partial Gradients $\nabla_{\vec{s}} J_i(\vec{s}, f)$ from Specific View Angles Using Equation (27) Compared to Parallel-Beam CT

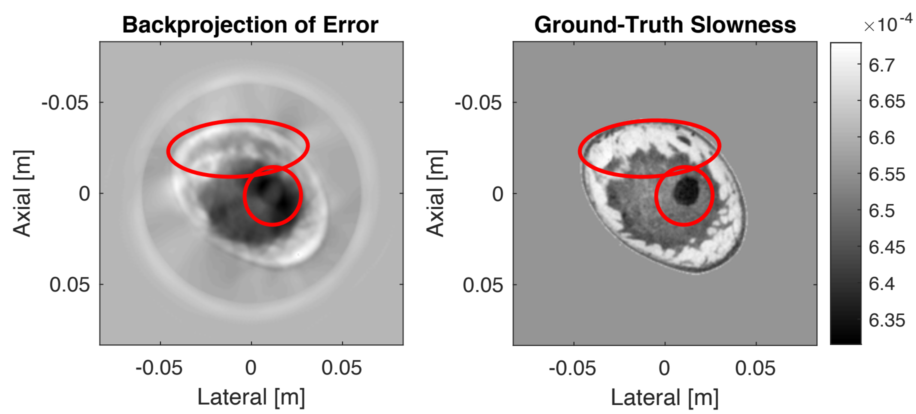

Figure 7. Complete Gradient Based on Accumulation of Partial Gradients from All View Angles and Frequencies: $\nabla_{\vec{s}} J(\vec{s}) = \sum_f \sum_{i=1}^{N_{views}} \nabla_{\vec{s}} J_i(\vec{s}, f)$. Including higher frequencies in the complete gradient results in cycle-skipping artifacts (examples are circled in red). Ground-truth slowness is given in units of seconds/meter

4.1 USCT Reconstruction

Figure 6 shows example gradient images (based on equation (27)) for the partial objective function $J_i(\vec{s}, f)$ at certain view angles in comparison to the backprojection from a parallel-beam computed tomography (CT) system.

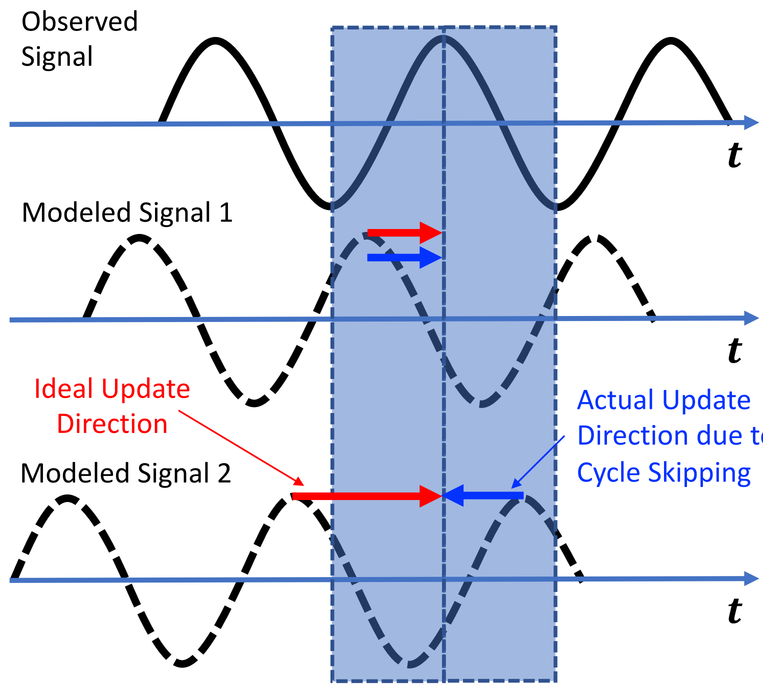

Figure 8. Visual Illustration of Cycle Skipping. Modeled Signal 1 simulates a medium with a slightly lower slowness (higher speed of sound) that than the ground-truth medium responsible for the Observed Signals. The difference between Modeled Signal 1 and the Observed Signal results in a positive update to the slowness estimate to advance the simulated wavefront. However, because Modeled Signal 2 simulates a much lower slowness than the ground truth medium, Modeled Signal 2 leads the Observed Signal by more than a half cycle (transparent blue boxes around central peak). As a result, the difference between Modeled Signal 2 and the Observed Signal results in a negative update to the slowness in the medium, aligning incorrect peaks in Modeled Signal 2 and the Observed Signal, even though the ideal update to the slowness should be positive.

These gradient images are effectively the backprojection of the error between the simulated and measured receive signals for these particular view angles at a 0.5 MHz transmit frequency. However, in comparison to parallel-beam CT where backprojection always occurs along straight line paths from sources to receivers, the backprojection in USCT is based on diffraction, which does not occur on straight-line paths. For this reason, if sources and receiver switch places, the backprojection image from USCT can change, unlike parallel-beam CT where sources and receivers are interchangeable.

The partial gradient images $\nabla_{\vec{s}} J_i(\vec{s}, f)$ in Figure 6 would be summed across view angles and frequencies to form the complete gradient $\nabla_{\vec{s}} J(\vec{s}) = \sum_f \sum_{i=1}^{N_{views}} \nabla_{\vec{s}} J_i(\vec{s}, f)$ as shown in Figure 7. However, when these gradient images are accumulated in frequency, cycle-skipping causes parts of the image to invert. Recall that according to equations (13) and (27), the gradient is computed by back-propagating the error between the simulated and measured receive signals. When simulated and measured receive signals are offset by more than half a cycle of the waveform, the error between the simulated and measured signals will induce updates to the slowness model in the direction opposing the optimal or preferred alignment of simulated and received signals (see Figure 8).

Figures 9 and 10 show the frequency-dependent effect of cycle skipping on the gradient computation. As frequency increases, cycle skipping causes the same misalignment between simulated and measured signals to increasingly update parts of the image in the opposite direction (Figure 9). Figure 10 is used to highlight cycle skipping in a particular region of the image based on the backprojection from a selected transmission angle. The slowness update in the circled region gradually inverts as the frequency increases. Figure 11 annotates each part of the simulated and measured signals for this transmission angle and relates errors between the simulated and measured signals to the backprojection image at that angle. Although parts of the slowness update behave

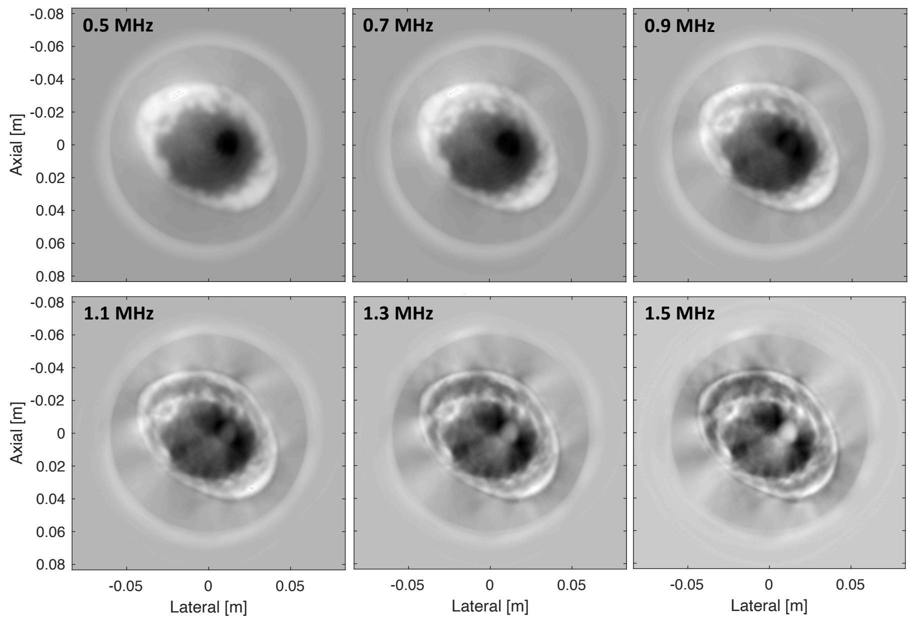

Figure 9. Frequency Decomposition of Gradient Image $\nabla_{\vec{s}} J(\vec{s})$. As the frequency increases, the effect of cycle skipping on the gradient image increases.

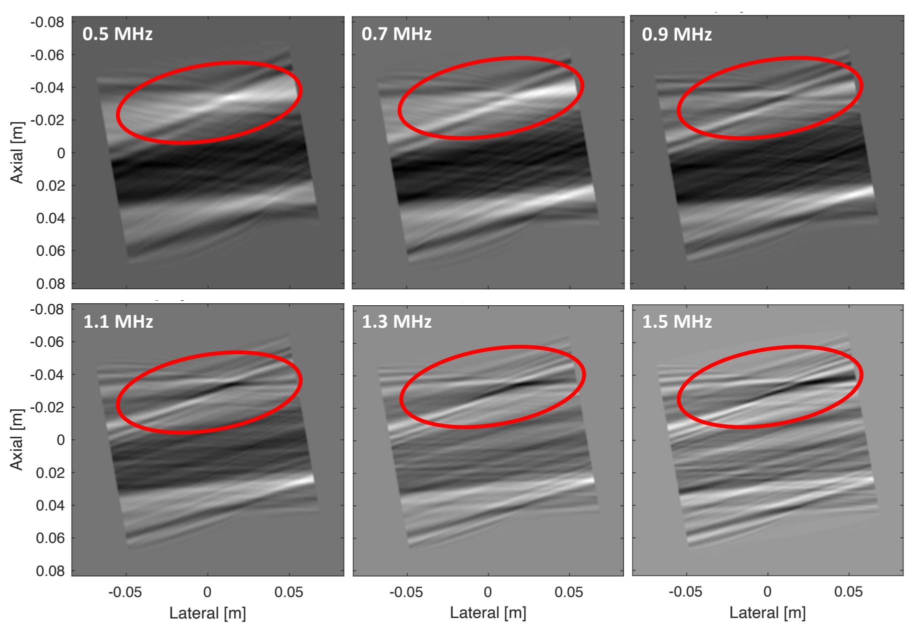

Figure 10. Frequency-Dependent Cycle-Skipping Artifact in Partial Gradient Image $\nabla J_i(\vec{s}, f)$ for Selected Transmission Angle. A specific region where cycle skipping becomes dominant as frequency increases is circled in red.

ideally according to whether the simulated signals lag or lead the measured signals, if the lag or lead is too large, parts of the image will update in the opposite direction based on cycle skipping.

When the conjugate gradient algorithm (Algorithm 1) is used to reconstruct the speed of sound in the medium, the damping factor γ plays a crucial role in stabilizing the reconstruction algorithm in the presence of cycle skipping artifacts. Cycle skipping is the main source of non-convexity in the waveform inversion problem.

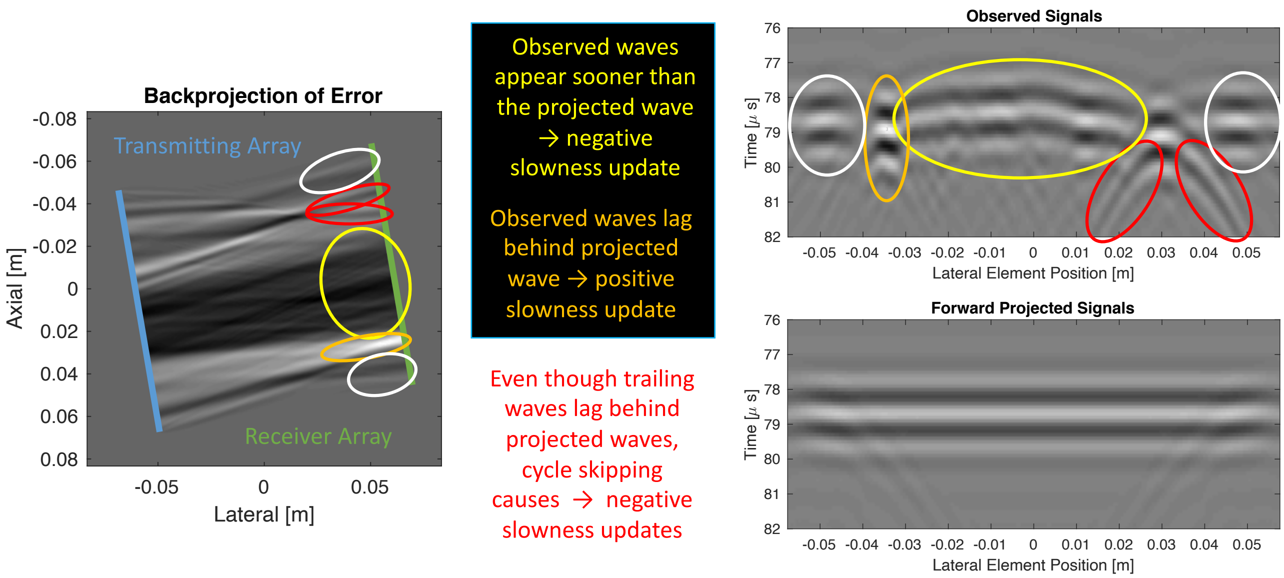

Figure 11. Explanation of Cycle-Skipping Artifact in Gradient Image for the Selected Angle of Transmission. When the measured signals appear sooner than the simulated signals, this indicates a negative update to the slowness image (circled in yellow). When the measured signals lag behind than the simulated signals, this indicates a positive update to the slowness image (circled in orange). However, if measured signals lag too far behind simulated signals (circled in red), cycle skipping induces negative updates to the slowness image even though positive updates would be ideal.

As opposed to true linear least-squares minimization problems, where conjugate gradient is typically implemented with a $\gamma = 1$ in its most standard form, waveform inversion inversion requires us to deliberately dampen or slow down the conjugate gradient method to prevent overshooting when cycle skipping occurs. Figure 12 shows the result of naively implementing the conjugate gradient method without damping ($\gamma = 1$). The result is that each step of the conjugate gradient method results in overshooting to compensate for the cycle skipping when determining the appropriate step size based on the linearized forward model. The instability of the conjugate gradient algorithm without damping causes the reconstruction to diverge. However, by damping the conjugate gradient method ($\gamma = 1$), the sound speed reconstruction converges to within 2.2 m/s RMS error after the same 12 iterations of the conjugate gradient method (Figure 13). By cutting down the size of each step in the conjugate gradient method, the reconstruction works around the parts of the image where cycle skipping occurs, and the cycle-skipping artifacts gradually disappear.

4.2 WEMVA Demonstration with Point Target Simulation

Figure 14(a) shows the pulse-echo reconstruction of a point target based on the cross-correlation of transmitted and received wavefields. The gradient of the magnitude of the reconstructed image with respect to slowness induces "wave" paths from each transmit element to the point target. When the individual gradients from each path are accumulated, we obtain the slowness gradient images shown in Figure 14(b).

Figure 14(b) shows the point target reconstruction and slowness gradient images when the focusing speed of sound is equal to the ground truth, less than the ground truth by 4%, and greater than the ground truth by 4%. When $c_{bfm} < c_{true}$ or $s_{bfm} > s_{true}$, a negative slowness update would be needed to optimally focus the point target to the correct location in space. However, the actual slowness gradient is negative only through its central portion while being positive laterally away from this central portion. Similarly, when $c_{bfm} > c_{true}$ or $s_{bfm} < s_{true}$, a positive slowness update would be needed to optimally focus the point target; however, the actual slowness gradient is only positive through its central portion while being negative lateral to this positive update.

This is because the goal of the slowness gradient is to optimally focus the point target in the image. These negative and positive slowness gradients correspond to the advancement and delay of spatially-migrated signals to

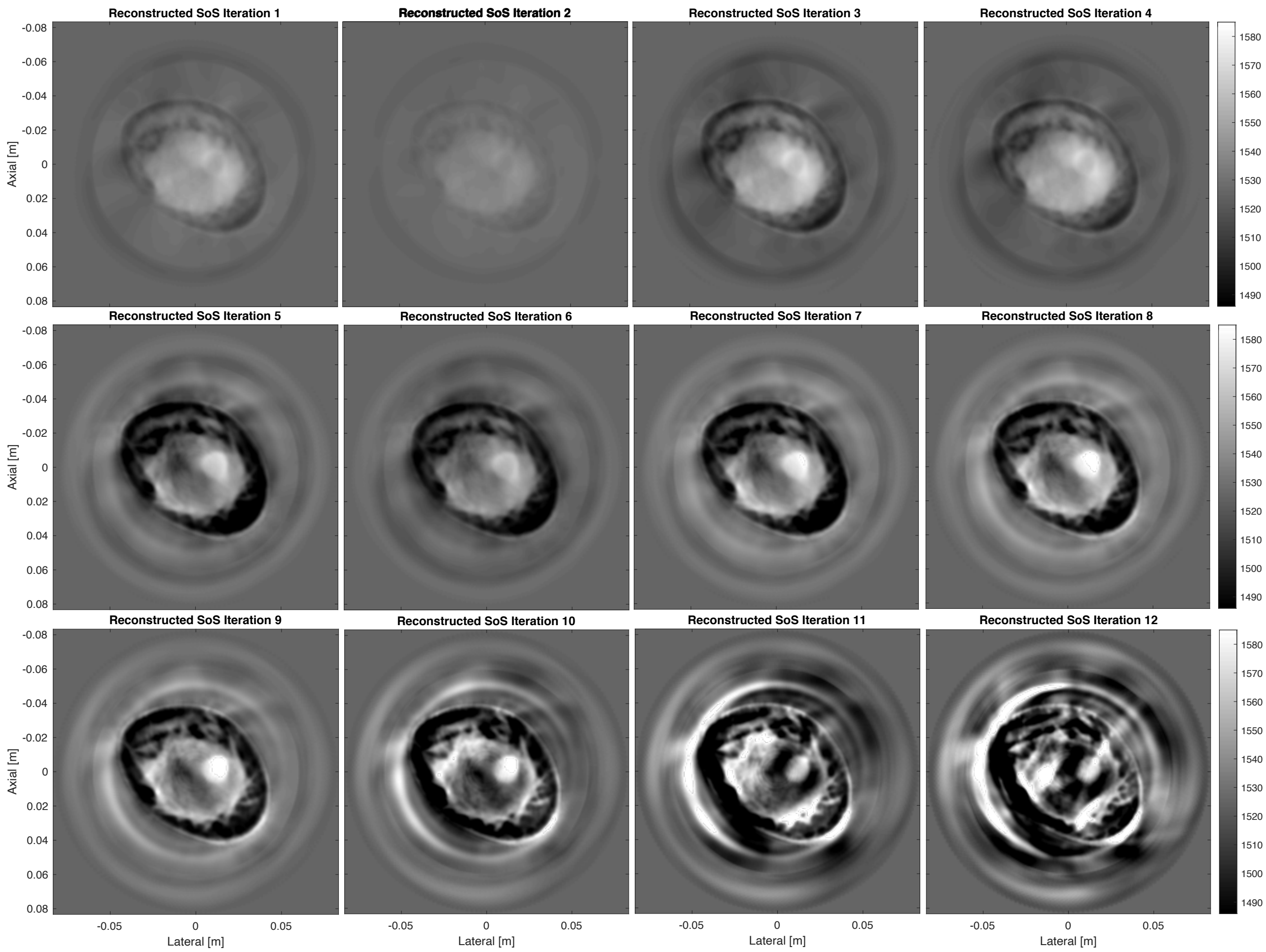

Figure 12. Conjugate Gradient Reconstruction of Sound Speed Without Damping ($\gamma = 1$). A naive implementation of the conjugate gradient algorithm without any damping factor results in the divergence of the reconstructed sound speed image. After 12 iterations, the algorithm continues to diverge from the ground-truth speed of sound.

produce a maximally focused point target at its current position in the image. In pulse-echo ultrasound imaging, the primary challenge of applying WEMVA to migrated signals when there is a bulk error in the speed of sound is the time-to-depth ambiguity. WEMVA will have initial difficulties in the depth placement of migrated targets because of this latent ambiguity. However, the hope is that successive iterations of WEMVA with multiple imaging targets using the conjugate gradient method should first resolve any laterally-varying component of the speed of sound in the medium and then slowly resolve axially-varying components in the speed of sound responsible for the depth placement of those imaging targets.

Figure 14(c) shows the same point target reconstruction and slowness gradient images when the linearized form of WEMVA is used. Recall that the linearized form of WEMVA is based on modeling the difference between migrated images from neighboring transmit elements. Because linearized WEMVA models the differences between neighboring transmit elements, the resulting gradient images are less smooth and have stronger edge effects due to the truncation of the aperture. However, the same effects seen in Figure 14(b) are seen Figure 14(c): when $c_{bfm} < c_{true}$ or $s_{bfm} > s_{true}$, there is a negative slowness update through the central portion of the gradient flanked by positive updates; when $c_{bfm} > c_{true}$ or $s_{bfm} < s_{true}$, there is a positive slowness update through the central portion of the gradient flanked by negative updates. Despite the rough appearance of the gradient images in Figure 14(c), previous work by[30] indicates that the integration of these gradients across multiple imaging targets leads to meaningful updates to the slowness model.

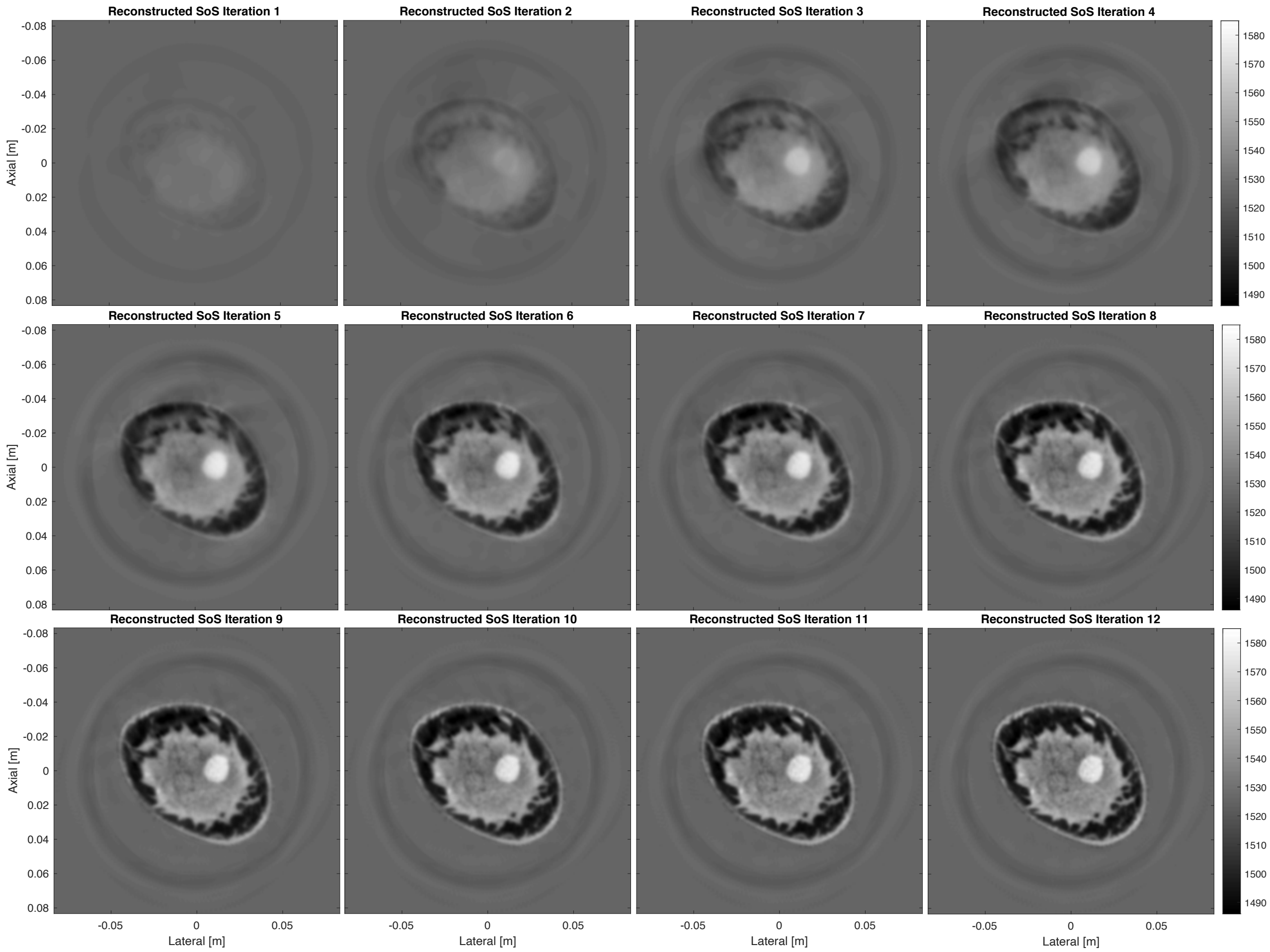

Figure 13. Conjugate Gradient Reconstruction of Sound Speed With Damping ($\gamma = 0.25$). By damping the step size, the conjugate gradient algorithm converges to the correction speed of sound after 12 iterations. The RMS error in between the final reconstruction and the ground-truth speed of sound is 2.2 m/s.

5. DISCUSSION AND CONCLUSIONS

Ultimately, the goal of this paper is to summarize, implement, and demonstrate the waveform inversion algorithm for transmission ultrasound computed tomography. We provide a complete open-source example of the waveform inversion algorithm on Github: https://github.com/rehmanali1994/FullWaveformInversionUSCT (DOI: 10.5281/zenodo.4774394).

The main distinction between waveform inversion tomography and conventional bent-ray or CT methods is the effect of cycle skipping. Although waveform inversion greatly outperforms bent-ray or arrival-time based CT methods for sound speed reconstruction, a major pitfall of waveform inversion is the effect of cycle skipping. Cycle skipping occurs when the time offset between simulated and measured signals is larger than a half-cycle of the waveform. This leads to erroneous updates to the slowness which lead to convergence issues in the reconstruction algorithm. To ameliorate the effects of cycle skipping on the reconstruction algorithm, each iteration of the conjugate gradient algorithm is damped to prevent overshooting at each slowness update (Algorithm 1). Previous works[4, 13] also employ a multi-scale approach where waveform inversion begins with the lowest frequencies in the waveform and proceed towards higher frequencies to improve the imaging resolution. As the commented in,[4, 13] the exact schedule regarding which frequencies are used to update the slowness estimate at each iteration is still an active area of research.

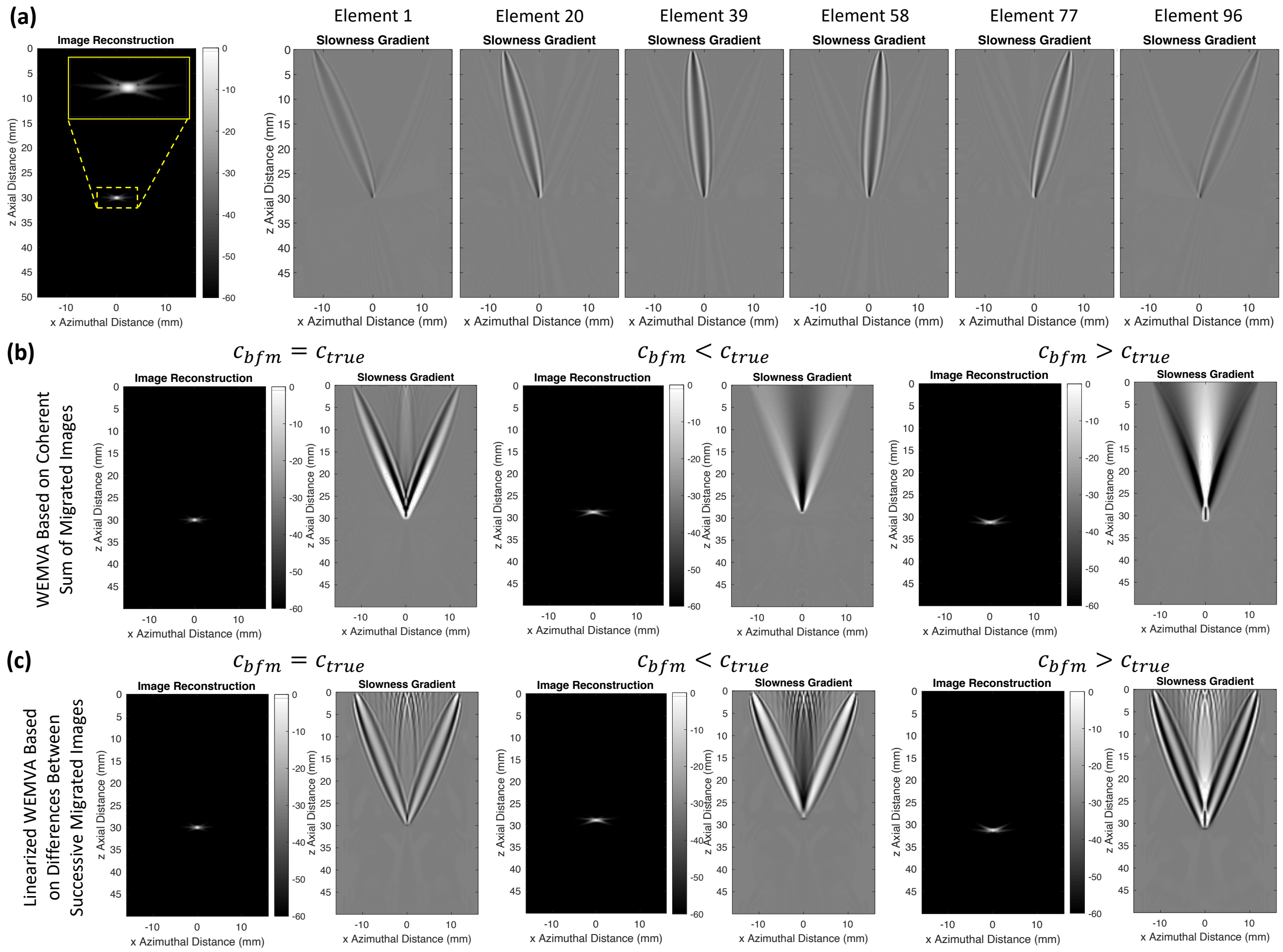

Figure 14. Slowness Gradients for the Pulse-Echo Reconstructions of a Point Target. (a) Point target image and wave paths induced between each transmit element and the point target when the image is focused at a sound speed c_{bfm} equal to the ground-truth sound speed $c_{true} = 1540$ m/s in the medium. (b) Point target reconstructions and slowness update direction images based on equation (44) when $c_{bfm} = c_{true}$, $c_{bfm} = 0.96c_{true}$, and $c_{bfm} = 1.04c_{true}$. This WEMVA implementation is based on the coherent sum of migrated images. (c) Point target reconstructions and slowness update direction images based on equation (49) when $c_{bfm} = c_{true}$, $c_{bfm} = 0.96c_{true}$, and $c_{bfm} = 1.04c_{true}$. Here, WEMVA is based on modeling the differences between migrated images from neighboring transmit elements.

This work also translates the same modeling framework used in waveform inversion to derive slowness updates for pulse-echo ultrasound imaging. The initial work presented here uses a point target to demonstrate two different implementations of wave-equation migration velocity analysis from seismic imaging. In each implementation, this work examines challenges such as the time-to-depth ambiguity involved in scaling the initial demonstration in point targets to more complex media using an iterative conjugate gradient algorithm (Algorithm 2). A complete demonstration of WEMVA for medical pulse-echo ultrasound imaging in more complex media is left to future work.

ACKNOWLEDGMENTS

The author would like to acknowledge Dr. Biondo Biondi and Joseph Jennings, from the Department of Geophysics at Stanford University, for their expertise and advice on waveform inversion and migration velocity analysis. The author would also like to acknowledge feedback from various faculty within the Stanford Radiological Sciences Laboratory (RSL) such as Dr. Jeremy Dahl and Dr. Adam Wang. Finally, the author would like to acknowledge the National Defense Science and Engineering Graduate (NDSEG) Fellowship for sponsoring his graduate research work.

REFERENCES

[1] Li, C., Duric, N., Littrup, P., and Huang, L., "In-vivo breast sound-speed imaging with ultrasound tomography," *Ultrasound in Medicine and Biology* **35**(10), 1615–1628 (2009).

[2] Duric, N., Littrup, P., Poulo, L., Babkin, A., Pevzner, R., Holsapple, E., Rama, O., and Glide, C., "Detection of breast cancer with ultrasound tomography: First results with the computed ultrasound risk evaluation (CURE) prototype," *Medical physics* **34**(2), 773–785 (2007).

[3] Schreiman, J., Gisvold, J., Greenleaf, J. F., and Bahn, R., "Ultrasound transmission computed tomography of the breast.," *Radiology* **150**(2), 523–530 (1984).

[4] Wiskin, J., Borup, D., Johnson, S., and Berggren, M., "Non-linear inverse scattering: high resolution quantitative breast tissue tomography," *The Journal of the Acoustical Society of America* **131**(5), 3802–3813 (2012).

[5] Kolb, T. M., Lichy, J., and Newhouse, J. H., "Occult cancer in women with dense breasts: detection with screening US–diagnostic yield and tumor characteristics.," *Radiology* **207**(1), 191–199 (1998).

[6] Kolb, T. M., Lichy, J., and Newhouse, J. H., "Comparison of the performance of screening mammography, physical examination, and breast US and evaluation of factors that influence them: an analysis of 27,825 patient evaluations," *Radiology* **225**(1), 165–175 (2002).

[7] Hormati, A., Jovanović, I., Roy, O., and Vetterli, M., "Robust ultrasound travel-time tomography using the bent ray model," in [*Medical Imaging 2010: Ultrasonic Imaging, Tomography, and Therapy*], **7629**, 76290I, International Society for Optics and Photonics (2010).

[8] Quan, Y. and Huang, L., "Sound-speed tomography using first-arrival transmission ultrasound for a ring array," in [*Medical Imaging 2007: Ultrasonic Imaging and Signal Processing*], **6513**, 651306, International Society for Optics and Photonics (2007).

[9] Wang, K., Matthews, T., Anis, F., Li, C., Duric, N., and Anastasio, M. A., "Waveform inversion with source encoding for breast sound speed reconstruction in ultrasound computed tomography," *IEEE transactions on ultrasonics, ferroelectrics, and frequency control* **62**(3), 475–493 (2015).

[10] Krebs, J. R., Anderson, J. E., Hinkley, D., Neelamani, R., Lee, S., Baumstein, A., and Lacasse, M.-D., "Fast full-wavefield seismic inversion using encoded sources," *Geophysics* **74**(6), WCC177–WCC188 (2009).

[11] Vyas, U. and Christensen, D., "Ultrasound beam simulations in inhomogeneous tissue geometries using the hybrid angular spectrum method," *IEEE transactions on ultrasonics, ferroelectrics, and frequency control* **59**(6), 1093–1100 (2012).

[12] Stolk, C. C. and de Hoop, M. V., "Modeling of seismic data in the downward continuation approach," *SIAM journal on applied mathematics* **65**(4), 1388–1406 (2005).

[13] Wiskin, J., Borup, D., Iuanow, E., Klock, J., and Lenox, M. W., "3-d nonlinear acoustic inverse scattering: Algorithm and quantitative results," *IEEE transactions on ultrasonics, ferroelectrics, and frequency control* **64**(8), 1161–1174 (2017).

[14] Pérez-Liva, M., Herraiz, J., Udías, J., Miller, E., Cox, B., and Treeby, B., "Time domain reconstruction of sound speed and attenuation in ultrasound computed tomography using full wave inversion," *The Journal of the Acoustical Society of America* **141**(3), 1595–1604 (2017).

[15] Ruiter, N. V., Zapf, M., Hopp, T., Gemmeke, H., and van Dongen, K. W., "Usct data challenge," in [*Medical Imaging 2017: Ultrasonic Imaging and Tomography*], **10139**, 101391N, International Society for Optics and Photonics (2017).

[16] Ruiter, N. V., Zapf, M., Hopp, T., Gemmeke, H., van Dongen, K. W., Camacho, J., Herraiz, J. L., Liva, M. P., and Udías, J. M., "Usct reference data base: conclusions from the first spie usct data challenge and future directions," in [*Medical Imaging 2018: Ultrasonic Imaging and Tomography*], **10580**, 105800Q, International Society for Optics and Photonics (2018).

[17] Sanabria, S. J., Ozkan, E., Rominger, M., and Goksel, O., "Spatial domain reconstruction for imaging speed-of-sound with pulse-echo ultrasound: simulation and in vivo study," *Physics in Medicine & Biology* **63**(21), 215015 (2018).

[18] Sanabria, S. J., Rominger, M. B., and Goksel, O., "Speed-of-sound imaging based on reflector delineation," *IEEE Transactions on Biomedical Engineering* (2018).

[19] Sanabria, S. J. and Goksel, O., "Hand-held sound-speed mammography based on ultrasound reflector tracking," in [*Medical Image Computing and Computer-Assisted Intervention–MICCAI 2016: 19th International Conference, Athens, Greece, October 17-21, 2016, Proceedings, Part I*], **9900**, 568–576, Springer International Publishing (2016).

[20] Vishnevskiy, V., Sanabria, S. J., and Goksel, O., "Image reconstruction via variational network for real-time hand-held sound-speed imaging," in [*International Workshop on Machine Learning for Medical Image Reconstruction*], 120–128, Springer (2018).

[21] Jaeger, M., Held, G., Peeters, S., Preisser, S., Grünig, M., and Frenz, M., "Computed ultrasound tomography in echo mode for imaging speed of sound using pulse-echo sonography: proof of principle," *Ultrasound in medicine & biology* **41**(1), 235–250 (2015).

[22] Ali, R., "Fourier-based synthetic-aperture imaging for arbitrary transmissions by cross-correlation of transmitted and received wave-fields," *Ultrasonic Imaging* **43**(5), 282–294 (2021).

[23] Schwab, H.-M., Ihrig, A., Depke, D., Hermann, S., Schäfers, M., and Schmitz, G., "Aberration correction in photoacoustic imaging using paraxial backpropagation," in [*2017 IEEE International Ultrasonics Symposium (IUS)*], 1–4, IEEE (2017).

[24] Schwab, H.-M. and Schmitz, G., "Full-wave ultrasound reconstruction with linear arrays based on a fourier split-step approach," in [*2018 IEEE International Ultrasonics Symposium (IUS)*], 1–4, IEEE (2018).

[25] Chen, B. and Stamnes, J. J., "Validity of diffraction tomography based on the first born and the first rytov approximations," *Applied optics* **37**(14), 2996–3006 (1998).

[26] Potvin, G., "General rytov approximation," *JOSA A* **32**(10), 1848–1856 (2015).

[27] Symes, W. W., "Migration velocity analysis and waveform inversion," *Geophysical prospecting* **56**(6), 765–790 (2008).

[28] Liu, Z. and Bleistein, N., "Migration velocity analysis: Theory and an iterative algorithm," *Geophysics* **60**(1), 142–153 (1995).

[29] Sava, P. and Biondi, B., "Wave-equation migration velocity analysis. i. theory," *Geophysical Prospecting* **52**(6), 593–606 (2004).

[30] Perrone, F., Sava, P., Andreoletti, C., and Bienati, N., "Linearized wave-equation migration velocity analysis by image warping," *Geophysics* **79**(2), S35–S46 (2014).

[31] Uhlig, J., Fischer, U., von Fintel, E., Stahnke, V., Perske, C., Lotz, J., and Wienbeck, S., "Contrast enhancement on cone-beam breast-ct for discrimination of breast cancer immunohistochemical subtypes," *Translational oncology* **10**(6), 904–910 (2017).